Corrosion Behavior of Alloy 625 in $PbSO_4$-Pb_3O_4-$PbCl_2$-ZnO-10 Wt Pct CdO Molten Salt Medium

E. MOHAMMADI ZAHRANI and A.M. ALFANTAZI

Corrosion behavior and degradation mechanisms of alloy 625 under a 47.288 $PbSO_4$-12.776 Pb_3O_4-6.844$PbCl_2$-23.108ZnO-10CdO (wt pct) molten salt mixture under air atmosphere were studied at 873 K, 973 K, and 1073 K (600 °C, 700 °C, and 800 °C). Electrochemical impedance spectroscopy (EIS), open circuit potential (OCP) measurements, and potentiodynamic polarization techniques were used to evaluate the degradation mechanisms and characterize the corrosion behavior of the alloy. Morphology, chemical composition, and phase structure of the corrosion products and surface layers of the corroded specimens were studied by scanning electron microscopy/energy-dispersive X-ray (SEM/EDX) and X-ray map analyses. Results confirmed that during the exposure of alloy 625 to the molten salt, chromium was mainly dissolved through an active oxidation process as CrO_3, Cr_2O_3, and $CrNbO_4$, while nickel dissolved only as NiO in the system. Formation of a porous and nonprotective oxide layer with low resistance is responsible for the weak protective properties of the barrier layer at high temperatures of 973 K and 1073 K (700 °C and 800 °C). There were two kinds of attack for INCONEL 625, including general surface corrosion and pitting. Pitting corrosion occurred due to the breakdown of the initial oxide layer by molten salt dissolution of the oxide or oxide cracking.

I. INTRODUCTION

HOT corrosion is a serious issue in power generation equipments, gas turbines, internal combustion engines, fluidized bed combustion, industrial waste incinerators, as well as paper and pulp industries, which could cause a significant reduction in the lifetime of the equipment and failure. Formation of low melting point deposited salts was deduced to be the main reason for the accelerated corrosion in waste to energy (WTE) boilers,[1–3] the wood-waste fluidized bed power boiler,[4] or the straw fired boiler.[5] Reportedly, hot corrosion attack in such boilers caused the formation of a porous and nonprotective oxide scale at the surface of the alloys.[6] Since 5 pct of the operating costs of these plants is attributed to the hot corrosion failure and related maintenance costs,[2,7] developing a better understanding of high-temperature corrosion phenomenon under molten salt environment in such plants is of high importance. Despite the fact that superalloys were developed for high-temperature applications, it should be noted that they are not always able to meet both the high-temperature strength and high-temperature corrosion resistance, simultaneously, in most applications.[8]

Phenomenologically, hot corrosion degradation of the alloys was characterized as a two-step process, namely, initiation and propagation. In the initiation stage, the response of the alloy to the corrosive environment is very similar to the behavior of the alloy in the absence of molten salt. However, at the second stage, as a result of deposit formation, the protective properties of the oxide scale are faced with a significant change compared to the properties of the oxide scale in the absence of the molten salt.[9,10] It was reported that the presence of chlorides in the deposits could accelerate the formation of low melting point eutectic phases, which could dissolve the protective oxide layer of the alloy through a gas phase active oxidation process.[11] In such cases, the corrosion rate mainly depends on the metal temperature, and this kind of corrosion was called "molten salt induced corrosion." Moreover, it is deduced that the amounts of Cl and SO_4 ions as well as alkaline and heavy metals alter the physical properties of the deposits, for example, the amount and permeability of the molten phase.[12]

The severity of the corrosion environments at the interface of metal/molten salt is influenced by the penetration depth of corrosive species through the scales, and it is reported that the protective effects of the oxide films, derived from alloying elements, play an important role in preventing the corrosion attack.[13] In the WTE environment, when the molten phase contains chlorine and sulfur, corrosion products of alloy 625 had lamellar structures, and the occurrence of oxidation, sulfidation, and chlorination was confirmed at the alloy/scale interface under a low partial pressure (P) of oxygen (P_{O_2})–high P_{Cl_2} condition.[13] In another study, Ishitsuka and Nose[14] reported that in the molten

E. MOHAMMADI ZAHRANI, Ph.D. Candidate, and A.M. ALFANTAZI, Professor and Associate Dean, are with the Corrosion Research Group, Department of Materials Engineering, University of British Columbia, Vancouver, BC V6T1Z4, Canada. Contact e-mail: ehsanmoh@interchange.ubc.ca

chloride and chloride/sulfate mixture, fast dissolution of Cr_2O_3 occurred, and it dissolved as a hexavalent chromium ion. In fact, in molten chloride environments, which could be mainly formed in WTE boilers, the dissolution of protective Cr_2O_3 films could occur through the chemical formation of CrO_4^{2-}.[14] In the presence of molybdenum, vanadium, or tungsten in the alloy, since these elements have a tendency to form their oxides on the surface of the alloy, $(P_{O_{2-}})$ of the molten salt at the interface will increase and the solubility of Cr_2O_3 will be expected to decrease. Therefore, these protective oxide films could assist Cr_2O_3 to protect the alloy against corrosive molten salt containing chlorine ions.[15] Obviously, these oxides could protect the substrate from the hot corrosion if they also demonstrate a low solubility in a molten salt corrosive environment, which is a somewhat basic solution especially in WTE boilers. Despite the fact that Fe_3O_4 is another oxide having low solubility in such a corrosive environment, it could not play the role of a protective oxide layer because of weak protective properties.[16]

Alloy 625 weld overlays possess excellent corrosion resistance and welding workability. Also, the application of corrosion-resistant materials such as INCONEL* 625

---

*INCONEL is a trademark of Special Metals Corporation, New Hartford, NY.

---

by means of the high velocity oxygen fuel thermal spray process or plasma spray is the best combination of erosion and corrosion resistance among several techniques.[2,17] The electrochemical impedance spectroscopy (EIS) technique was used to study the corrosion behavior of alloy 625 beneath the $ZnCl_2$-KCl salt mixture at 923 K (650 °C) up to 200 hours by Perez et al.[18] According to the results, the corrosion process was controlled by the transition of ions in the oxide scale, and EIS profiles were fitted to a protective scale model before 100 hours and to a porous scale model at higher exposure times.[18] Because of the Zn and Nb diffusion from molten salt and alloy, respectively, both $ZnCr_2O_4$ and $NbCrO_4$ were found as corrosion products.[18]

In this study, the corrosion performance and degradation mechanisms of alloy 625 under the lead sulfate-lead (II,IV) oxide-lead chloride-zinc oxide-10 wt pct cadmium oxide molten salt system at 1073 K, 973 K, and 873 K (800 °C, 700 °C, and 600 °C) were studied by using EIS, OCP, and potentiodynamic polarization techniques. The formation of corrosive molten salt mixture with this chemical composition and these phase characteristics is prevalent on the water-wall tubes of the radiant boiler in KIVCET lead and zinc smelters, where alloy 625 is commonly used to protect water-wall tubes of the boiler against molten salt-induced corrosion and

to reduce the corrosion rate of the boiler tubes.[8] However, there is no report on the electrochemical behavior and corrosion mechanism of alloy 625 in this environment.

II. EXPERIMENTAL PROCEDURE

Alloy 625 samples, used in the present work as working electrode, had a rectangular shape with $20 \times 10 \times 2$ mm dimensions. The chemical composition of the material, in weight percent, which was determined by inductively coupled plasma analysis/atomic absorption spectroscopy (ICP/AAS) (Inspectorate-International Plasma Laboratory (IPL), Richmond, BC, Canada), can be seen in Table I. Rectangular pieces of alloy 625 were ground to 1200 grit silicon carbide paper, rinsed with distilled water, ultrasonically degreased with acetone, and dried under a warm air stream. For preparation of the working electrode, a wire made of 80 wt pct Cr-20Ni was spot welded to each sample to provide the electrical connection between the working electrode and the potentiostat. For isolating the 80Cr-20Ni wire from the molten salts, alumina tubes were used, and the gap between the ceramic tube and the electrical connection wire was filled with refractory cement.

Analytical-grade $PbSO_4$ and CdO (Sigma-Aldrich, St. Louis, MT), Pb_3O_4 (Alfa Aesar, Ward Hill, MA), $PbCl_2$, and ZnO (Fisher Scientific, Hampton, NH) were used for preparing the salt mixture. For preparation of the salt mixture, measured amounts of the necessary chemical compounds (Table II) were added into a container and then milled for 3 days to prepare a homogeneous salt mixture. Specific amounts of the prepared salt mixture (15 g/cm^2 of the initial area of the specimen) were introduced into a 30 mL alumina crucible, to give a melt depth of about 3.5 cm. Then, the crucible was set inside an electrical vertical furnace to reach the test temperature, which was measured constantly during the tests using a type K thermocouple under the static air atmosphere. The crucible together with the solid corrosive salts was replaced for each experiment. The potentiostat used in the electrochemical experiments was a Princeton Applied Research (PAR) model 273 A with M352 analysis software.

Open circuit potential (OCP), potentiodynamic polarization, and EIS were conducted in the molten

Table II. Chemical Composition (Weight Percent) of the Salt Mixture

	$PbSO_4$	$PbCl_2$	Pb_3O_4	ZnO	CdO
Salt mixture	47.288	6.844	12.776	23.108	10

Table I. Chemical Composition (Weight Percent) of Alloy 625

Ni	Cr	Mo	Fe	Nb	Ti	Sb	Zn	Al	C	S	Si
55.08	20.97	8.30	4.50	2.80	0.16	0.20	0.25	0.44	0.15	0.02	0.31

salt mixture at 1073 K, 973 K, and 873 K (800 °C, 700 °C, and 600 °C) in a three electrode cell. In all techniques, the electrochemical cell was constituted by the working electrode (alloy 625) and two 1.2-mm diameter/500-mm long platinum wires as auxiliary and quasi-reference electrodes. Platinum wires were woven together to produce a meshlike counterelectrode (CE). The meshlike CE to working electrode (WE) surface ratio was equal to 5 (CE:WE = 5:1). All platinum electrodes were cleaned, abraded by using 600 grit SiC sand paper, washed, and dried before being isolated in the ceramic tubes and sealed with the refractory cement, leaving 5-mm-long free length to make contact with the corrosive molten salt. Once the crucible containing the salt mixture was set into the electrical tube furnace, the electrochemical cell was introduced inside the crucible, and the corresponding cables of the potentiostat were connected to the electrochemical cell. Instrument connections were made well away from the furnace to avoid thermocouple effects. OCP was recorded at the first 24 hours of the test. Before performing the potentiodynamic polarization and EIS tests, the OCP of the cell must reach a stable value and the system should be at equilibrium condition. Afterward, impedance measurements were carried out in the frequency range from 50 kHz to 1 mHz with an AC voltage amplitude of ±5 mV with respect to the OCP. Then, the working electrode potential was continuously increased from −200 to +1200 mV with respect to the OCP at a scan rate of 1 mV/s in potentiodynamic polarization tests. The selection of this sweep rate was also reported by other researchers.[19–21] Scanning electron microscopy (SEM) on a Hitachi S-3000N (Tokyo, Japan) electron microscope with light metal energy-dispersive X-ray spectroscopy (EDX) was used to study the surface and cross section of the samples after electrochemical tests. Phase analysis of the corrosion products on the surface of the samples was studied by the X-ray diffraction (XRD) technique using a Rigaku MultiFlex X-ray diffractometer and using Ni-filtered Cu K_α ($\lambda_{Cu K_\alpha}$ = 0.154186 nm, radiation at 40 kV and 20 mA) over the 2θ range of 20 to 60 deg (scan speed: 2 deg per minute, and step size: 0.04 deg). For phase analysis, the obtained XRD patterns were compared to the standards compiled by the Joint Committee on Powder Diffraction and Standards (JCPDS) to identify phases.

III. RESULTS AND DISCUSSION

A. OCP Measurements

In a corrosion cell, potential of working electrode *vs* reference electrode when no potential or current is being applied to the cell is known as OCP. In the literature, the OCP is also called zero-current potential or rest potential.[22] In order to study some aspects of the kinetics and mechanism of the electrode processes,[23] for example, passive layer or anodic film growth, stability or dissolution, monitoring the OCP *vs* time can be used.

OCP changes as a function of time at 873 K, 973 K, and 1073 K (600 °C, 700 °C, and 800 °C) can be seen in Figure 1. At the beginning of the test, the potential of the electrode increased together with some variations and then reached a steady state. This indicates that the corrosion resistance of the alloy increased with time and eventually reached a relatively stable value because of the formation of a passive film. In the OCP curves at 873 K and 973 K (600 °C and 700 °C), the potential of the electrodes increased for 45 minutes and then reached a quasi–steady state. This rapid increase in the potential of the electrode exposed to the molten salt at 873 K and 973 K (600 °C and 700 °C) could be attributed to the spontaneous growth of a passive film on the surface of the electrode in these two temperatures. Steady-state OCP of the electrode at 973 K and 873 K (700 °C and 600 °C) was found to be 7 and 12 mV, respectively. At 1073 K (800 °C), the OCP curve fluctuated during the first 19 hours of exposure to the molten salt and afterward reached a quasi–steady state. Steady-state OCP of the electrode was equal to 5.7 mV, very close to the steady-state OCP at 973 K (700 °C). The fluctuation at the first 19 hours of exposure to the molten salt at 1073 K (800 °C) could be attributed to the unstable nature of the passive film, formed on the surface of the electrode.

B. Potentiodynamic Polarization Study

The potentiodynamic polarization method has been widely used as a powerful technique for general corrosion testing and measurement of the corrosion rate of different alloys in the molten salt medium.[8,19–21] Figure 2 showed the potentiodynamic polarization curves at 873 K, 973 K, and 1073 K (600 °C, 700 °C, and 800 °C) after 24 hours of exposure, when OCP reached a stable value, indicating electronic conductivity in the salt. Also, corrosion current density (i_{corr}), corrosion potential, and cathodic Tafel slope, which were extracted from potentiodynamic polarization data through the Tafel extrapolation technique,[22] as well as calculated corrosion rate (mm/year) values, can be seen in Figure 2. The corrosion potential of the alloy 625
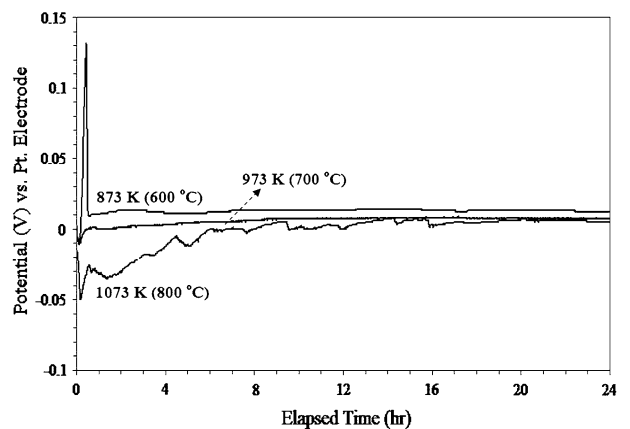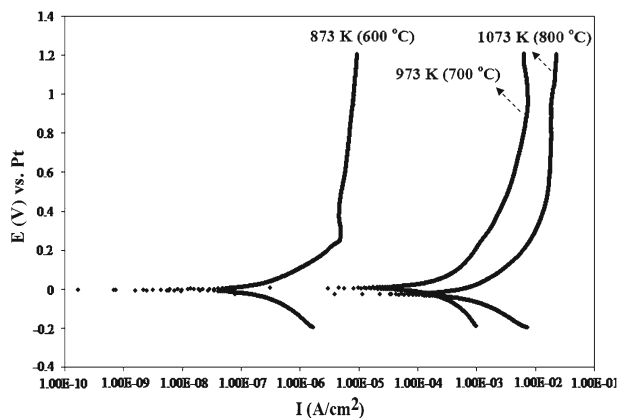

Fig. 1—OCP of alloy 625 electrode, exposed to the molten salt mixture at 873 K, 973 K, and 1073 K (600 °C, 700 °C, and 800 °C).

Temperature K (°C)	β_C (mV.dec^{-1})	I_{corr} $^{(Tafel)}$ (mA.cm^{-2})	Corrosion Rate (mm / year)	E_{corr} (mV)
1073 (800)	179.389	2.89	63.532	- 26.935
973 (700)	372.472	1.081	23.764	5.057
873 (600)	276.859	0.001	0.022	- 3.661

Fig. 2—Potentiodynamic polarization curves of alloy 625 electrode, exposed to the molten salt mixture at 873 K, 973 K, and 1073 K (600 °C, 700 °C, and 800 °C).

electrode in the molten salt mixture at 873 K, 973 K, and 1073 K (600 °C, 700 °C, and 800 °C) was determined to be −3.66, 5.06, and −26.94 mV vs Pt, respectively. Except for the E_{corr} value at 973 K (700 °C), which is positive, E_{corr} values at 873 K and 1073 K (600 °C and 800 °C) are negative and obviously the most active E_{corr} belongs to 1073 K (800 °C). In fact, it suggests that a smaller deriving force was required to initiate the corrosion of alloy 625 at 1073 K (800 °C). It was clear that by increasing the temperature, the corrosion rate of the alloy increased (Figure 2) and the potentiodynamic polarization curves shifted toward the left-hand side of the diagram. In fact, the corrosion activity increased with an increase in the temperature because of an increase in the electrical conductivity of the molten salt mixture as well as a reduction in the viscosity of the molten salt, thus favoring the diffusion of chemical active species.[8] Tafel slopes lower than 100 mV/dec were typical for activation-controlled systems, whereas Tafel slopes with higher values were typical for systems that are not purely activation and diffusion controlled.[19,24] Considering the anodic branch of the potentiodynamic polarization curves, it could be suggested that alloy 625 could form an oxide film at all investigated temperatures. The oxide film seems to be less protective at the higher temperatures (973 and 1073 K (700 and 800 °C)) due to a significant increase in the anodic current density by increasing the temperature.[25] At the potentiodynamic polarization curve of the 873 K (600 °C), in the potentials higher than +0.25 mV up to +1.2 mV, the anodic current density was almost constant in a wide potential region. Due to this relatively stable anodic current density in a wide potential range, oxide film (anodic film) can be described as a passivelike layer. The oxide layer, which formed at 873 K (600 °C) on the alloy surface, was more protective compared to the 973 K and 1073 K (700 °C and 800 °C) due to the lower corrosion rate of the alloy at 873 K (600 °C). Phase structure, morphology, and chemical composition of anodic passivelike layers will be discussed in Sections III–D and III–E.

C. EIS Study

The electrochemical corrosion behavior of alloy 625 was modeled based on the obtained data from the EIS technique, and excellent agreement between the model and experimental data was observed. The impedance behavior of the alloy 625 electrode, including measured and calculated Nyquist plots, and bode diagrams of phase angle and total impedance magnitude at 873 K, 973 K, and 1073 K (600 °C, 700 °C, and 800 °C) are presented in Figure 3. Considering the surface and cross-sectional morphology of alloy 625 after the electrochemical tests, as will be extensively discussed in Section III–E, two electrochemical models were developed and EIS data were fitted into two equivalent circuits. The electrochemical circuits of these two developed models as well as model parameters for equivalent circuits at each temperature can be seen in Figure 4. At 1073 K and 873 K (800 °C and 600 °C), Nyquist diagrams show two depressed capacitive loops, including a small loop in the high frequency range and a big loop in the low frequency range. The corresponding phase angle vs frequency curves had one relatively symmetrical maximum in the low frequency range. The capacitive loops may be related to the dielectric properties of the Cr-rich porous layer formed on the electrode surface at 1073 K and 873 K (800 °C and 600 °C). The equivalent circuit of the porous scale model at 1073 K and 873 K (800 °C and 600 °C) belongs to the alloy suffering from localized fast corrosion attack (pitting) in the molten salt environment, as can be seen in Figures 6 and 7. In this model, R_{dl} and R_{sl} represent charge transfer resistance along the localized corrosion zone (porous zone) and transfer resistance of ions in the scale layer, respectively. A porous scale model was suggested by Perez et al.[18] to explain Nyquist plots for the corrosion of alloy 625 in a molten $ZnCl_2$-KCl mixture at 923 K (650 °C). In this case, the corrosion mechanism was controlled by diffusion of the aggressive ions through the alloy/melt interface.[18] At 973 K (700 °C), two depressed semicircles were distinguishable in the Nyquist diagram, and an obvious linear region followed the second capacitive loop and measured EIS data were fitted into a two nonprotective and porous scale layers model (Figures 3 and 4). The linear region of the Nyquist diagram could be attributed to molten phase mass-transfer effects and Warburg-type behavior when the frequency is lower than 3.4 mHz. This linear region diminished as the temperature decreased to 873 K (600 °C); probably, the resistance of the scale layer increased at lower temperatures and masked the linear region. Also, this linear region disappeared when the temperature increased to 1073 K (800 °C), because diffusion of the aggressive species at the interface of the alloy and molten salt

becomes faster and diffusion of the oxidants could not act as a rate-controlling step at 1073 K (800 °C). The phase angle *vs* frequency curve (973 K (700 °C)) had one maximum and one shoulder at the high and low frequency ranges, respectively. According to Figure 4, the charge transfer resistance of the outer scale layer (R_{osl}) at 973 K (700 °C) and charge transfer resistance of scale layer (R_{sl}) at 1073 K (800 °C) are both quite low, and these layers could not act as effective protective barrier layers. This fact was confirmed by the high

corrosion rate of alloy 625 at 1073 and 973 K (800 and 700 °C) (Figure 2). However, the charge transfer resistance of the scale layer (R_{sl}) at 873 K (600 °C) is high, and it shows that the scale layer of the alloy at 873 K (600 °C) can reasonably play the role of an effective protective barrier layer and reduce the corrosion rate of the alloy at 873 K (600 °C) compared to 973 K and 1073 K (700 °C and 800 °C).

At all investigated temperatures, the phase angle maxima were much smaller than 90 deg. Carranza and
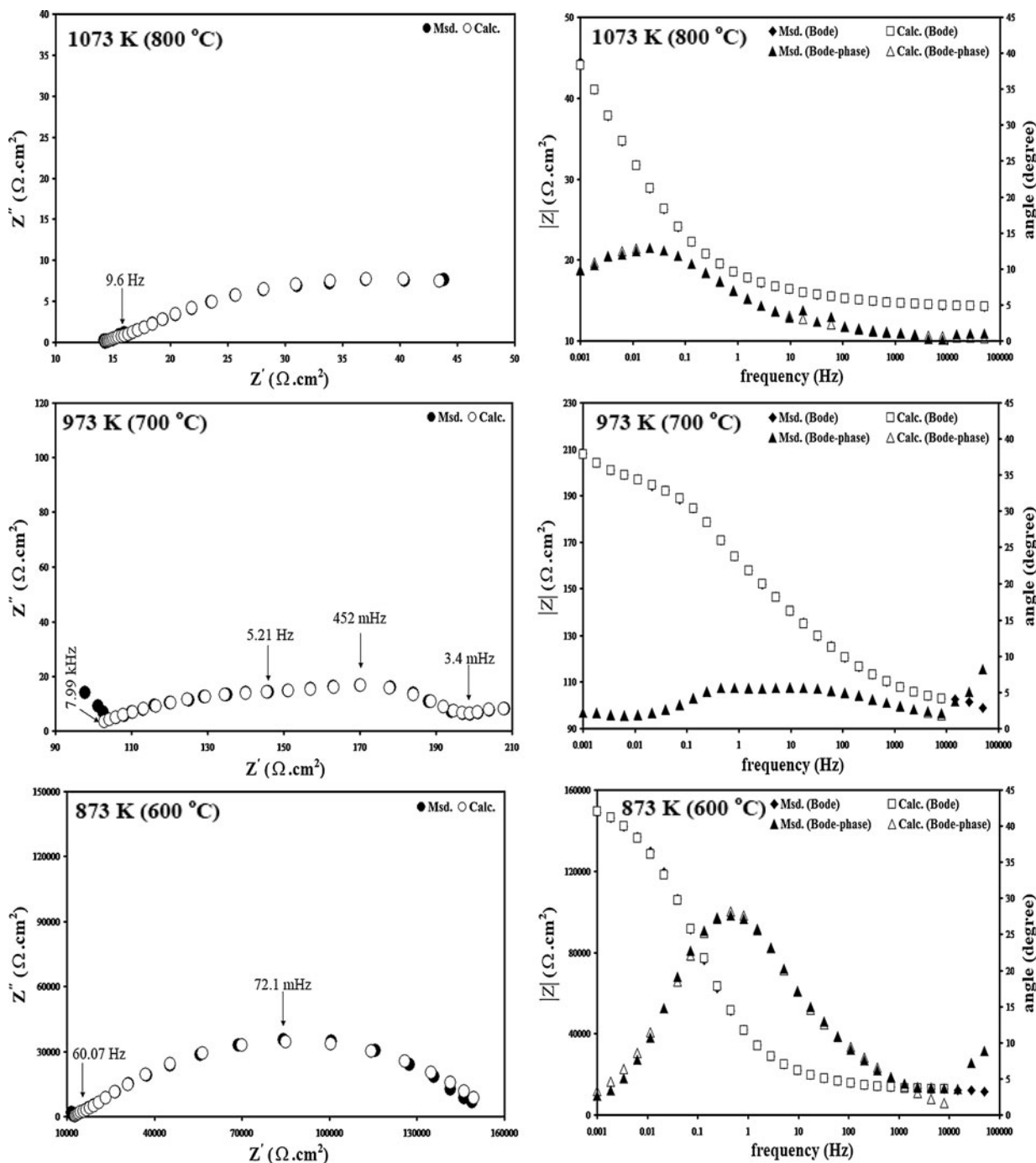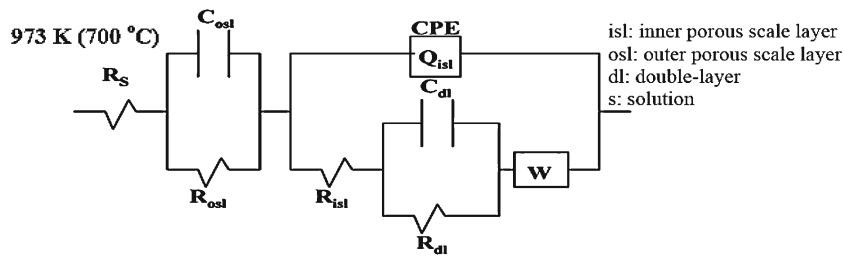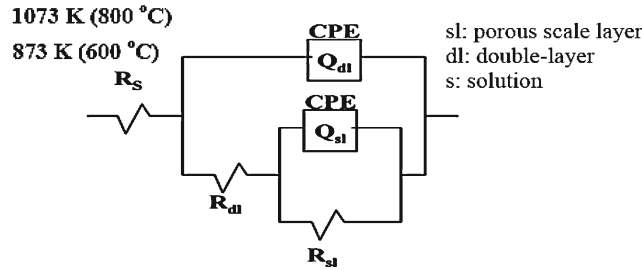

Fig. 3—EIS Nyquist plots response plus bode diagrams of phase angle and total impedance magnitude for alloy 625, exposed to molten salt mixture at 873 K, 973 K, and 1073 K (600 °C, 700 °C, and 800 °C).

Parameter / Temperature	R_s ($\Omega.cm^2$)	R_{osl} ($\Omega.cm^2$)	C_{osl} ($F.cm^{-2}$)	R_{isl} ($\Omega.cm^2$)	Q_{isl}-Yo ($S.sec^n.cm^{-2}$)	Q_{isl}-n	R_{dl} ($\Omega.cm^2$)	C_{dl} ($F.cm^{-2}$)	W ($S.sec^{0.5}.cm^{-2}$)	χ^2
973 K (700 °C)	97.44	10.98	0.04585	99.29	0.003058	0.322	11.2	12.92	0.0002296	8.35×10^{-6}

Parameter / Temperature	R_s ($\Omega.cm^2$)	R_{dl} ($\Omega.cm^2$)	Q_{dl}-Yo ($S.sec^n.cm^{-2}$)	Q_{dl}-n	R_{sl} ($\Omega.cm^2$)	Q_{sl}-Yo ($S.sec^n.cm^{-2}$)	Q_{sl}-n	χ^2
1073 K (800 °C)	14.16	7.05	0.07424	0.3438	43.83	0.04967	0.5718	7.854×10^{-5}
873 K (600 °C)	12350	11420	0.000004549	0.562	133200	0.000007669	0.5961	3.064×10^{-4}

Fig. 4—Equivalent electrochemical circuits at 973 K (700 °C) (two nonprotective scale layers model), 1073 K (800 °C), and 873 K (600 °C) (porous scale layer model) beneath molten salt mixture plus the model's parameters of equivalent circuits for alloy 625 exposed to molten salt mixture.

Alvarez explained that surface roughness, frequency dispersion of time constants due to local inhomogeneities in the dielectric material, porosity mass transport effects, and relaxation effects could be some reasons for this phenomenon.[26] In the present study, the most probable reason for having phase angles much smaller than 90 deg could be the frequency dispersion of time constants due to the local inhomogeneities in the dielectric material, because of the inhomogeneous nature of the molten salt mixture. Also, for bode plots of 973 K and 873 K (700 °C and 600 °C), the diagrams showed straight lines with slopes smaller than −1 at high frequency range. This feature could be related to the frequency dispersion, and it can be attributed to the solid surface inhomogeneities.[27] Beverskog et al. mentioned that the number of distinguishable maxima or related shoulders was an indication of the minimum number of relaxation processes (time constants) that occurred in the electrochemical system, which were detectable through the EIS technique.[28] Therefore, the EIS results exhibited a minimum of one time constant at 1073 K and 873 K (800 °C and 600 °C), but a minimum of two relaxation processes and time constants at 973 K (700 °C). At 973 K (700 °C), the relaxation process at the high frequency range may be attributed to the growth of the outer porous scale layer, and at the same time, the relaxation process at the low frequency range may be related to the growth of the inner porous scale layer.[29,30] In Figure 3, the values of both real and imaginary impedance rose with decreasing temperature in the molten salt, resulting in an increase of the impedance modulus and the radius of the capacitive loop. This confirmed the decrease of corrosion rates observed in polarization measurements (Figure 2). R_s, the solution resistance between the working and reference electrode, and R_{ct} (R_{dl}), the charge transfer resistance of the diffusion-controlled reaction, both significantly increased by decreasing the temperature. This phenomenon may be explained considering the fact that the viscosity of the molten salt significantly decreased as a result of an increase in temperature, while the mass fraction of the molten phase increased, simultaneously. These two factors could enhance the diffusion of the aggressive species from the molten environment toward the molten phase/electrode surface interface and, subsequently, accelerate the corrosion of the alloy.

D. XRD Analysis

In order to develop an understanding of the corrosion products and scale layer phase structure, formed on the surface of the alloy after electrochemical studies, the surface of the alloy 625 corroded samples was studied by the XRD technique. The obtained XRD patterns from the scale layers formed on the surface of the samples, which were exposed to the molten salt mixture at 873 K, 973 K, and 1073 K (600 °C, 700 °C, and 800 °C), are
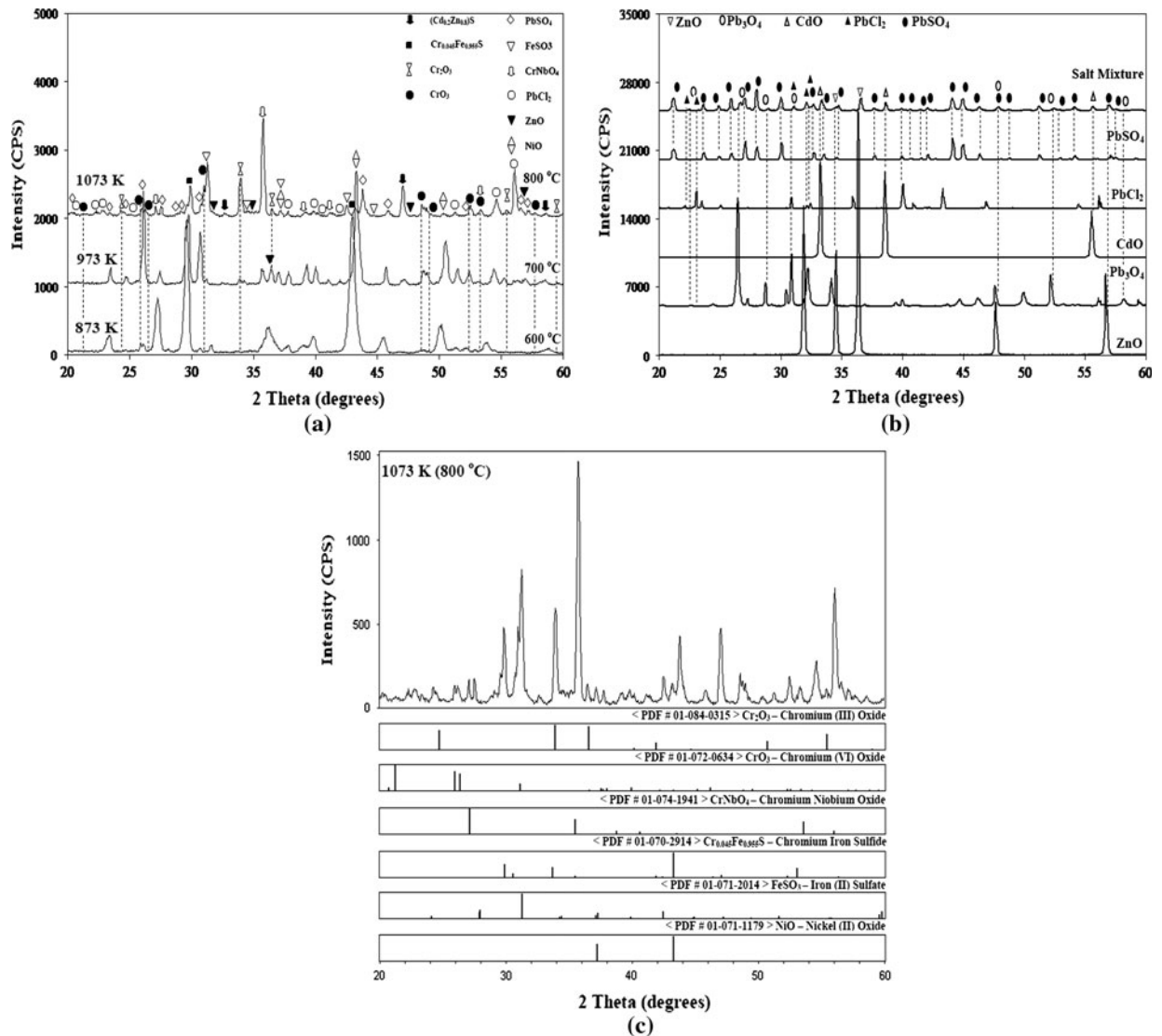
Fig. 5—XRD patterns of (*a*) corrosion products formed on the surface of alloy 625 after electrochemical tests at 873 K, 973 K, and 1073 K (600 °C, 700 °C, and 800 °C), (*b*) initial salts and prepared salt mixture, and (*c*) corrosion products formed on the surface of the alloy 625 after electrochemical tests at 1073 K (800 °C) in comparison with standard XRD patterns of the components, compiled by JCPDS.

presented in Figure 5(a). Also, the XRD patterns of the initial salts (listed in Table II) as well as the prepared salt mixture can be seen in Figure 5(b) for comparison. In the XRD pattern of 1073 K (800 °C), in addition to the residue salts such as $PbSO_4$ (JCPDS 01-089-7356), $PbCl_2$ (JCPDS 01-084-1177), ZnO (JCPDS 01-075-1526), and $(Cd_{0.2}Zn_{0.8})S$ (JCPDS 01-071-4155), which deposited on the surface of the electrode, Cr_2O_3 (JCPDS 01-084-0315), CrO_3 (JCPDS 01-072-0634), $FeSO_3$ (JCPDS 01-071-2014), $CrNbO_4$ (JCPDS 01-074-1941), NiO (JCPDS 01-071-1179), and $(Cr_{0.045}Fe_{0.955})S$ (JCPDS 01-070-2914) phases were detectable in the scale layer. In Figure 5(c), the XRD pattern at 1073 K (800 °C) was compared with the standard XRD patterns (JCPDS file) of the major corrosion products. By decreasing the temperature, major peaks of CrO_3 and Cr_2O_3 disappeared and the others became significantly weak. Ultimately, no obvious and well-developed characteristic peaks of Cr_2O_3 phase were detectable in the

XRD pattern of 873 K (600 °C). Meanwhile, the characteristic peaks of the NiO became more intensified by decreasing the temperature. Another important observation was the detection of $FeSO_3$ and $(Cr_{0.045}Fe_{0.955})S$ in the scale layer as a result of the iron sulfidation process during corrosion in molten salt. The formation of these two phases confirmed that iron, which was present in alloy 625 (Table I), could be dissolved in the molten salt through sulfidation reaction. However, active oxidation of Cr and Ni, two major alloying elements in alloy 625, appeared to be the main degradation mechanism.

Formation of $(Cr_{0.045}Fe_{0.955})S$ phase indicated that a sulfidation reaction also could have contributed to the Cr dissolution. Niobium is another alloying element in the chemical composition the alloy 625, with a tendency for participation in the active oxidation reactions because of the presence of $CrNbO_4$ in the XRD patterns. However, the presence of MoO_2 was not
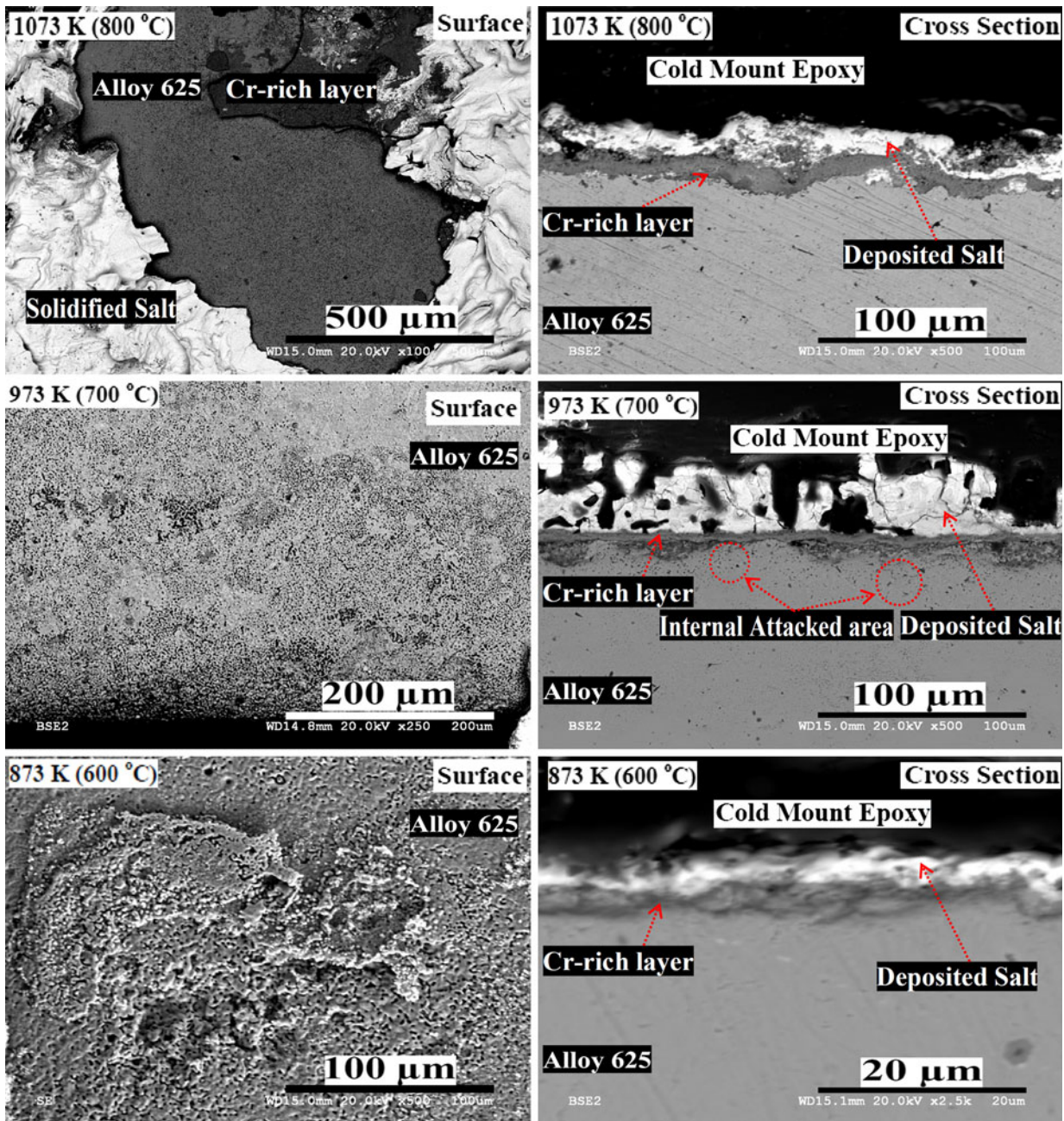
Fig. 6—SEM photomicrographs of alloy 625 substrates, exposed to the molten salt mixtures (after corrosion tests), which show the surface and cross section of the corroded samples.

identified by XRD. The formation of $CrNbO_4$ in the scale layer was also reported by Perez *et al.* during the corrosion of alloy 625 in the $ZnCl_2$-KCl molten salt mixture at 923 K (650 °C).[18] Hence, active oxidation and sulfidation appeared to be the two major mechanisms occurring at the substrate/melt interface to selectively dissolve the substrate alloying elements and cause the corrosion attack.[31] Based on the phase composition of the scale layer formed on the surface of the alloy after the tests, the active oxidation is the main degradation mechanism in alloy 625 under the molten salt system of the present study. XRD results confirmed that the metal ions Fe^{+2}, Ni^{+2}, Cr^{+3}, and

Cr^{+6} react with the oxide ions to form metal oxides. Because of the occurrence of such oxidation reactions, the oxygen concentration was increased near the surface of the alloy, which could enhance oxygen diffusion into the alloy from the atmosphere through the molten salt to form oxide.

E. SEM/EDX Analysis

Figures 6 and 7 present SEM photomicrographs from the surface and cross section of alloy 625 at different magnifications and SEM imaging modes, backscattered electron (BSE) and secondary electron (SE), after
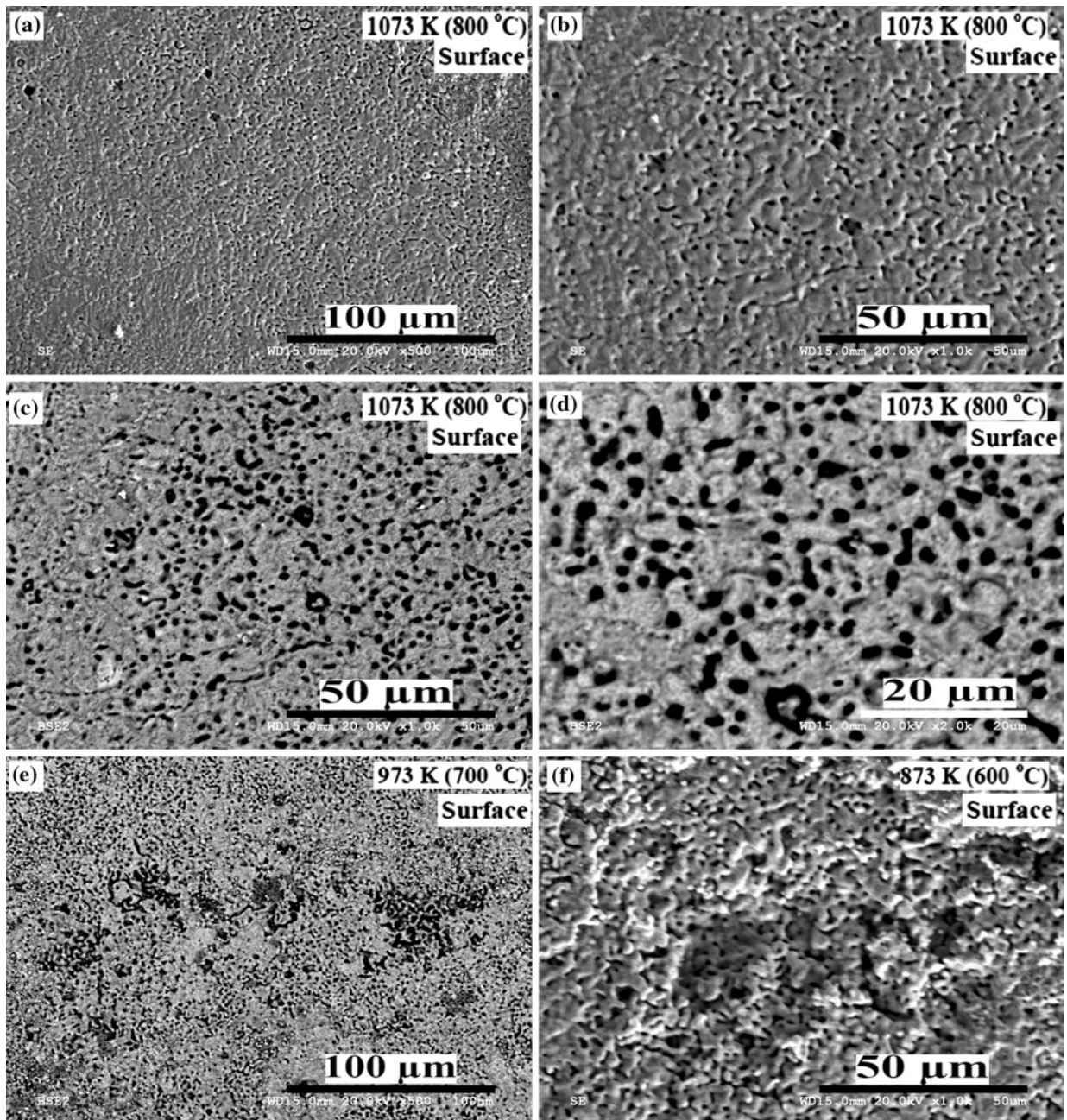
Fig. 7—SEM photomicrographs of the surface of alloy 625 substrates, exposed to the molten salt mixtures (after corrosion tests), which illustrate SE images at (*a*) 500 times and (*b*) 1000 times magnification, (*c*) BSE mode of image (*b*) at the same magnification for comparison purposes, (*d*) BSE image at 2000 times magnification, (*e*) BSE image at 500 times magnification, and ultimately, (*f*) SE image at 1000 times magnification. General surface corrosion and pitting, as two main modes of corrosion attack, are obvious in these images.

exposure to the molten salt mixture in corrosion tests at 873 K, 973 K, and 1073 K (600 °C, 700 °C, and 800 °C). Corrosion products and a thick Cr-rich oxide layer, together with some pores and pits under the Cr-rich layer (internal attacked area), were formed at the surface of the substrate at 1073 K and 973 K (800 °C and 700 °C).

Based on the SEM results, there appeared to be two types of attack for INCONEL 625, including general surface corrosion and pitting. A comparison, which was made between SE and BSE modes of an image in

Figures 7(b) and (c), is obvious evidence of the presence of pores and pits on the attacked surfaces after exposure to the molten salt medium. Pitting corrosion occurred due to the breakdown of the initial protective oxide layer by molten salt dissolution of the oxide or crack formation in the oxide layer. Montgomery *et al.* mentioned that chloride and sulfates present as heavy metal salts in the melt or semimelt phase could be responsible for pitting corrosion.[32] It seems that because of the nonprotective nature of the Cr-rich oxide layer, which was formed on the surface of the alloy at 973 K and
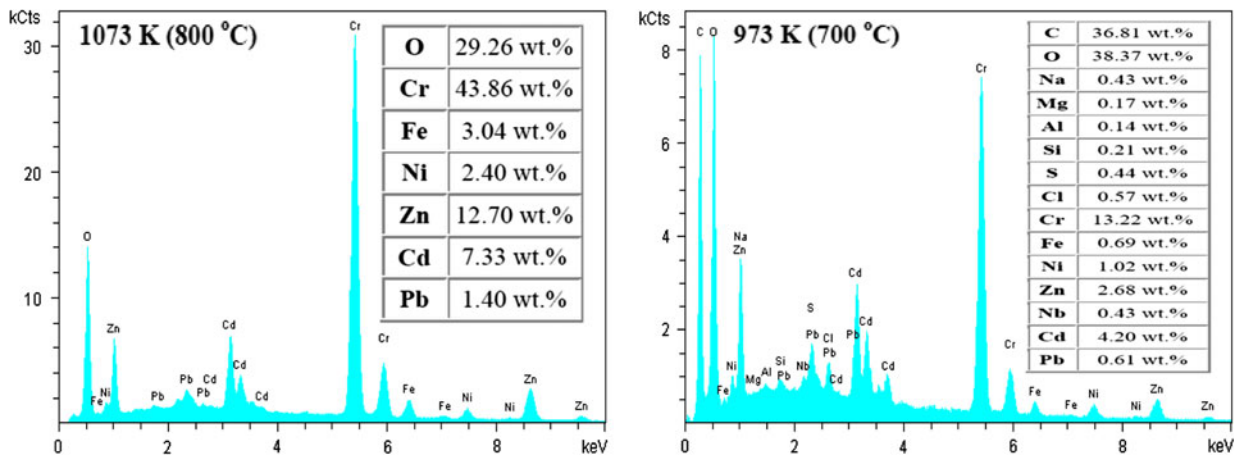
Fig. 8—EDX analysis from the outer surface of the scale layer formed on the surface of alloy 625 substrate, exposed to the molten salt mixture (after corrosion test).

1073 K (700 °C and 800 °C), corrosive species diffused in the alloy from the surface during exposure to the molten salt and caused the intergranular corrosion process (internal attacked area).[8] The internal attacked area was not formed under the interface of the Cr-rich oxide layer and alloy at 873 K (600 °C), so the oxide layer formed on the surface of the substrate at 873 K (600 °C) could be considered an effective protective oxide layer, not a corrosion product layer (Section III–A). The mean thickness of the oxide layers at 873 K, 973 K, and 1073 K (600 °C, 700 °C, and 800 °C), measured by using SEM photomicrographs, was equal to 2.464 ± 0.503 μm, 7.879 ± 2.959 μm, and 10 ± 2.609 μm, respectively. As can be seen by increasing the temperature, the thickness of the oxide layers rose.

EDX analysis from the outer surface of the scale layer, formed on the surface of the substrate at 973 K and 1073 K (700 °C and 800 °C), can be seen in Figure 8. Cr content (dissolved from the substrate) of this layer was equal to 43.9 and 13.2 wt pct at 1073 K and 973 K (800 °C and 700 °C), respectively. This result was in a good agreement with the higher corrosion rate of alloy 625 in the molten salt environment at 1073 K (800 °C) than at 973 K (700 °C) (Figure 2). Because of the significant amount of oxygen in the chemical composition, it is plausible to claim that Cr was dissolved into the molten phase during the active oxidation reactions at the interface of the substrate and the molten salt, which was in a good agreement with the results of XRD analysis.

X-ray maps for Cr, Ni, and O at the interface of the substrate and molten phase at 973 K and 1073 K (700 °C and 800 °C) were presented in Figure 9. Ni and Cr mapping showed that the Ni-rich layer, formed on top of the Cr-rich layer, was denser and thicker at 973 K (700 °C) than at 1073 K (800 °C). The formation of the two Ni- and Cr-rich oxide layer on the surface of the alloy at 973 K (700 °C) was in a good agreement with the results of the EIS plots (Figures 3 and 4), which showed two depressed semicircle capacitive loops in the Nyquist diagram of 973 K (700 °C). Based on the Ni, Cr, and O mapping in Figure 9, it was clear that in the

bode plot of the sample at 973 K (700 °C) (Figure 3), the relaxation process at the high frequency range was attributed to the growth of the outer Ni-rich oxide barrier layer, and the simultaneous relaxation process at low frequency range was related to the growth of the inner Cr-rich oxide barrier layer. Also, Ni, Cr, and O mapping confirmed the presence of dissolved Cr and Ni in the molten salt composition in the form of oxide, in the areas that were away from the substrate/molten salt interface. EDX analysis of the Cr-rich layer (area close to the Cr-rich layer/alloy interface) confirmed that at 1073 K (800 °C), the concentration of Cr (46.5 wt pct) was higher compared to that at 973 K (700 °C) (34.6 wt pct), while the concentration of the Ni was higher (8.2 wt pct) at the 973 K (700 °C). It means that at 1073 K (800 °C), the tendency of Cr for participation in the active oxidation reaction at the interface of the alloy and molten salt was higher, which was in good agreement with the XRD results.

IV. CONCLUSIONS

In the current study, the corrosion behavior and degradation mechanisms of alloy 625 beneath 47.288 $PbSO_4$-12.776 Pb_3O_4-6.844 $PbCl_2$-23.108 ZnO-10 CdO (wt pct) molten salt mixture under air atmosphere were studied at 873 K, 973 K, and 1073 K (600 °C, 700 °C, and 800 °C) by EIS, OCP, and potentiodynamic polarization techniques. Alloy 625 could form an anodic film after 24 hours of exposure to the molten salt. The oxide film was a protective layer at 873 K (600 °C), while the oxide film should be regarded as a corrosion product film with decreased resistance at temperatures of 973 K and 1073 K (700 °C and 800 °C). The EIS analyses showed a relaxation process in the low frequency range at 1073 K and 873 K (800 °C and 600 °C), while it showed two relaxation processes at 973 K (700 °C). The relaxation process at the high frequency range was attributed to the growth of the outer Ni-rich oxide barrier layer, and at the same time, the relaxation process at low frequency range was related to the growth
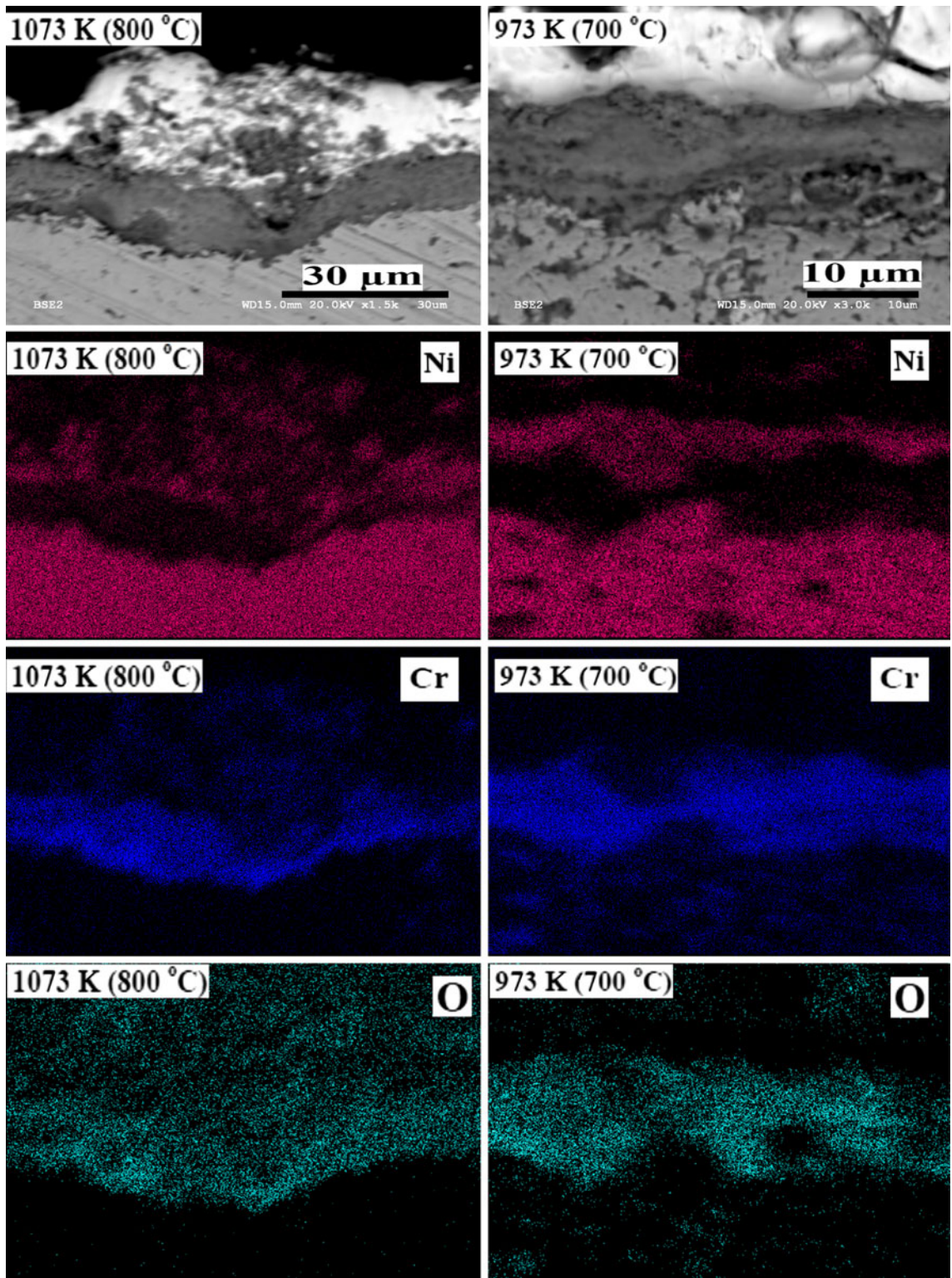
Fig. 9—X-ray mapping of Cr and Ni and EDX analysis of the cross section of the alloy 625 substrate, exposed to the molten salt mixtures (after corrosion tests).

of the inner Cr-rich oxide barrier layer. During the corrosion process, Cr was mainly dissolved in an active oxidation process as CrO_3, Cr_2O_3, and $CrNbO_4$, while Ni dissolved only as NiO in the system. Fe and a small portion of Cr also participated in a sulfidation reaction at the molten salt/metal interface. Formation of a porous and nonprotective oxide layer with decreased resistance was responsible for the weak protective properties of the barrier layer at high temperatures of 973 K and 1073 K (700 °C and 800 °C). There were two

types of attack for INCONEL 625, including general surface corrosion and pitting. Pitting corrosion occurred due to the breakdown of the initial oxide layer by molten salt dissolution of the oxide or oxide cracking.

REFERENCES

1. Y. Kawahara: *J. Thermal Spray Technol.*, 2007, vol. 16 (2), pp. 202–13.
2. S.-H. Lee, N.J. Themelis, and M.J. Castaldi: *J. Thermal Spray Technol.*, 2007, vol. 16 (1), pp. 104–10.
3. S.-H. Lee, N.J. Themelis, and M.J. Castaldi: Internal Report, University of New York, 2006, pp. 1–11.
4. J.R. Kish, D.L. Singbeil, P. Eng, O. Posein, and R. Seguim: *Corrosion*, 2007, vol. 63, pp. 197–204.
5. H.P. Michelsen, F. Frandsen, K.D. Johnson, and O.H. Larson: *Fuel Process. Technol.*, 1998, vol. 54, pp. 95–108.
6. R.A. Rapp and Y.S. Zhang: *JOM*, 1994, vol. 46, pp. 47–55.
7. H. Zwaher: *11th North America WTE Conf.*, Tampa, FL, 2003.
8. E. Mohammadi Zahrani, C. Cuevas-Arteaga, D. Verhelst, and A. Alfantazi: *Electrochem. Soc. Trans.*, 2010, vol. 28 (24), pp. 171–85.
9. M.H. Li, X.F. Li, Z.Y. Zhang, T. Jin, H.R. Guan, and Z.Q. Hu: *Oxid. Met.*, 2003, vol. 59, pp. 591–605.
10. T.S. Sidhu, R.D. Agrawal, and S. Prakash: *Surf. Coat. Technol.*, 2005, vol. 198, pp. 441–46.
11. Y. Kawahara: *Proceedings of the Japan Institute of Metals Annual (JIM) Conference*, The Japan Institute of Metals, Japan, ISBN 4-88903-129-4, 2001, p. 39.
12. Y. Kawahara and M. Kira: *Zairyo-to-Kankyo*, 1997, vol. 46, pp. 8–17.
13. Y. Kawahara: *Corros. Sci.*, 2002, vol. 44, p. 223.
14. T. Ishitsuka and K. Nose: *Corros. Sci.*, 2002, vol. 44, pp. 247–63.
15. B.P. Montany and D.A. Shores: *Corros. Sci.*, 2004, vol. 46, pp. 2893–2907.
16. H.J. Grabke, M. Spiegel, and A. Zhas: *Mater. Res.*, 2004, vol. 7, pp. 89–95.
17. J. Kalivodova, D. Baxter, M. Schultze, and V. Rohr: *Mater. Corros.*, 2008, vol. 59, pp. 367–73.
18. F.J. Perez, J. Nieto, J.A. Trilleros, and M.P. Hierro: *Mater. Sci. Forum*, 2006, vols. 522–523, pp. 531–38.
19. C. Cuevas Arteaga: *Corros. Sci*, 2008, vol. 50, pp. 650–63.
20. C. Cuevas-Arteaga, U. Uruchurtu, J. González, G. Izquierdo-Montalvo, J. Porcayo Calderón, and U. Cano-Castillo: *Corrosion*, 2004, vol. 60 (6), pp. 548–60.
21. C. Cuevas-Arteaga, J. Porcayo-Calderón, G. Izquierdo, and A.V. Martínez: *Mater. Sci. Technol.*, 2001, vol. 17, pp. 880–85.
22. A.J. Bard and L.A. Faulkner: *Electrochemical Methods: Fundamentals and Applications*, 2nd ed., John Wiley and Sons Inc., New York, NY, 2001, pp. 5–9.
23. A.G. Zelinsky, B.Y. Pirogov, and O.A. Yurjev: *Corros. Sci.*, 2004, vol. 46, pp. 1083–93.
24. W. Skinner: *Br. Corros. J.*, 1987, vol. 22 (3), pp. 172–75.
25. H. Sun, X. Wu, and E.-H. Han: *Corros. Sci.*, 2009, vol. 51, pp. 2565–72.
26. R.M. Carranza and M.G. Alvarez: *Corros. Sci.*, 1996, vol. 38, pp. 909–25.
27. K. Hladky, L.M. Callow, and J.L. Dawson: *Br. Corros. J.*, 1980, vol. 15, pp. 20–25.
28. B. Beverskog, M. Bojinov, A. Englund, P. Kinnunen, T. Laitinen, K. Mäkelä, T. Saario, and P. Sirkiä: *Corros. Sci.*, 2002, vol. 44, pp. 1901–21.
29. J.J. Park, S.I. Pyun, and S.B. Lee: *Electrochim. Acta*, 2004, vol. 49, pp. 281–92.
30. B. Rosborg and J. Pan: *Electrochim. Acta*, 2008, vol. 53, pp. 7556–64.
31. R.A. Rapp: *Corros. Sci.*, 2002, vol. 44, pp. 209–21.
32. M. Montgomery, O. Biede, and O.H. Larsen: *Mater. Sci. Forum*, 2006, vols. 522–523, pp. 523–30.